




# A High Altitude Platform-Based 3D Geometrical Channel Model for Beamforming Characterization in Future 6G Flying Ad-Hoc Networks

Muhammet Kırık , Liza Afeef , and Hüseyin Arslan , *Fellow, IEEE*

**Abstract**—Growing requirements of future wireless communication systems, such as high data rates, high reliability, and low latency, make the active usage of Non-Terrestrial Networks (NTN) an inevitable necessity. In this regard, High Altitude Platforms (HAPs) have drawn great attention in recent years due to their unique characteristics such as high coverage, long operational durability, and ad-hoc movement. However, for the active usage of HAPs, channel models for their various usage scenarios must be well-defined, especially in those cases where the sophisticated multiple-input multiple-output (MIMO) techniques, such as beamforming, are utilized to increase the data rate. Therefore, in this study, an air-to-air (A2A) three dimensional (3D) geometrical channel model is proposed to characterize the beamforming capabilities of non-stationary HAP networks operating at millimeter wave (mmWave) frequency band. In this regard, the 3D geometry of the two HAPs in the air is analyzed, and the effect of Doppler due to the movement of HAPs is interrogated as well as its effect on the signal-to-noise ratio (SNR). The final outputs of this study show that the proposed A2A channel model is applicable to characterize the future sixth generation (6G) HAP networks when the mmWave is used to utilize beamforming with a large number of antennas.

**Index Terms**—FANET, HAP, UAV, channel model, NTN, MIMO, Beamforming, Antenna Array.

## I. INTRODUCTION

**D**UE to the uneven distribution of Internet of Things (IoT) devices and internet users in various environments, such as urban centers, hilly terrains, rural villages, vast oceans, and many other challenging environments, ensuring adequate coverage becomes a crucial factor in providing high Quality of Service (QoS) [1]. In this regard, fifth generation (5G) has introduced the usage of NTN for the first time and identified the characteristics of New Radio (NR) in NTN to eradicate the possible challenges on the way to provide full coverage [2], [3]. However, even though there are some early initiatives to implement NTN into existing communication networks, it does not appear like the current 5G standards that are mainly composed of terrestrial Base Stations (BSs) will provide a satisfactory solution to cover the entire surface of the Earth in the 6G era [4].

On the other hand, the adoption of mmWave and MIMO systems in 5G and 6G networks is motivated by the growing demand for wireless communication and the scarcity of available spectrum caused by the proliferation of connected

devices and Internet applications [5]. With the introduction of 5G, mmWave, operating in the 30-300 GHz range, is harnessed to provide abundant bandwidth, low latency, and gigabit-speed connectivity for billions of devices [6]. However, exploiting the mmWave spectrum presents challenges such as pathloss, penetration loss, shadowing, atmospheric attenuation, and hardware limitations. In response, both industry and academia have worked on innovative MIMO techniques and channel models to enable the use of mmWave in outdoor 5G cellular networks.

Implementing mmWave and MIMO technologies on HAP communication systems can improve the spectral efficiency. However, within the advent of the 6G era, the requirement for novel transmission techniques and channel models for long-distance non-terrestrial air-to-air (A2A) and air-to-ground (A2G) applications, is more than ever to complete the vision of the 5G and prepare the world for the next generation communication networks.

In this regard, this paper analyses and models the beamforming usage at mmWave band in a scenario where two HAPs communicate through an A2A channel. It should be noted that the majority of A2A/A2G channel models proposed in the literature are developed for low altitude Unmanned Aerial Vehicles (UAVs). However, HAPs have their unique advantages that make them more preferable than both spaceborne terminals such as Low Earth Orbit (LEO) satellites or low altitude airborne UAVs such as drones. Therefore, the proposed channel model is considered on the basis of HAPs' communication.

### A. Literature Review

In this subsection, some of the related state-of-the-art works in the literature are reviewed with their potential and limitations.

In [7], a geometrical A2A channel model is presented for UAV communication. Although the proposed channel model provides some enlightening insights about non-stationary UAV networks, this model misses the opportunity to investigate the characteristics of mmWave band. Differing from [7], the work in [8] and [9] represents a geometrical A2A channel model for non-stationary UAV networks that utilize mmWave MIMO technology. Even though the proposed channel model in these works provides some valuable insights about the utilization of mmWave band with MIMO in non-stationary UAV communications, the characterization of beamforming,

The authors are with the Department of Electrical and Electronics Engineering, Istanbul Medipol University, 34810 Istanbul, Turkey (e-mail: muhammet.kirik@medipol.edu.tr; liza.shehab@std.medipol.edu.tr; huseyinarslan@medipol.edu.tr).

which is one of the key techniques for the usage of higher frequency bands, is not conducted by the authors.

*Dabiri et al.* in [10] provided an elaborate channel model analysis for UAV networks using a geometrical approach. The work focuses on three scenarios: an A2A link scenario, a ground-to-air-to-ground link scenario, and a scenario where the communication between two UAVs is amplified by a UAV that serves as a relay in the middle. The proposed channel models for these scenarios are conducted under the assumption that the UAVs are capable of performing directional beamforming by deploying multiple antenna elements. However, the model ignores the mobility of the UAVs and focuses on a hovering scenario which leaves some unlit areas that can be observed only in mobile scenarios such as Doppler shift, beam shift, etc.

Moreover, some channel models for low-altitude A2A and A2G communication links are presented in [11]–[15] along with some channel models for HAP networks given in [16]–[18]. Although the existing A2A literature is heavily based on low-altitude airborne terminals, which provides some insight into the channel characteristics of inter-HAP communication links they cannot be adopted directly to characterize the high-altitude A2A channel for HAPs networks.

## B. Contributions

The contributions of this paper can be listed as follows:

- i.) At higher frequency bands such as mmWave, characteristics of the channel heavily depend on environmental factors such as scatterers and reflectors. This is due to the fact that the short wavelength at these bands causes the signal to act as a beam and deviate from its direction rather than creating a multipath. To characterize these deviations, geometrical channel models are heavily used in the literature rather than deterministic or stochastic channel models. As stated earlier, the characteristics of low altitude UAVs and HAPs cannot be evaluated by the same channel model due to their environmentally identifying differences. Due to the fact that at the altitude that HAPs operate the possible scatterers and reflectors such as constructions, vehicles, clouds, etc. do not exist, the geometry of the transmitted signal beam is required to be specifically analysed for HAPs. Therefore, this paper provides an elaborate 3D geometrical channel model analysis for those scenarios where two non-stationary HAPs communicate through an A2A channel at mmWave band and the beamforming is performed on the transmitted signal;
- ii.) A comprehensive mobility model is proposed for HAPs that takes into account the altitude, speed, and trajectory. The model allows the characterization of the unrestricted movement capabilities of HAPs, which is essential for understanding their behavior in the presence of various environmental factors. This contribution provides a tool for predicting and optimizing the performance of HAPs based on their movement characteristics;
- iii.) The paper mathematically analyzes MIMO and beamforming characteristics between a transmitter and receiver HAP, and consolidates the results with simulations.

Specifically, the authors investigate the impact of the relative positions, orientations, and beamforming parameters of the two HAPs on the quality of the communication link. Beamforming is a critical technique for enhancing the performance of wireless communication systems, and the analysis conducted in this paper provides insight into how it can be used to optimize HAP networks;

- iv.) The paper investigates the effect of Doppler on the performance of the received signal when the beam direction is misaligned. The authors consider both the angular and frequency components of the Doppler effect and examine how they affect the quality of the received signal. Doppler can cause significant degradation in the performance of wireless communication systems, and the analysis in this paper provides a better understanding of how it impacts HAP networks. The results of this analysis can be used to inform the design of more robust communication systems that can mitigate the effects of Doppler;

## C. Organization

The rest of this paper is organized as follows. In Section II, the system model of the proposed channel model is given by explaining the operation scenario in detail, providing a mobility model, and interrogating the effect of Doppler due to mobility. In Section III, the performance metrics of the proposed channel model are mathematically analyzed. In Section IV, the mathematical analyses are continued by deriving the probabilistic characteristics of the proposed channel model. In Section V, the simulation results of the proposed channel model are shown along with a discussion. Lastly, in Section VI, the paper is concluded.<sup>1</sup>

## II. SYSTEM MODEL

### A. Transceiver Model

In this scenario, it is considered that the two highly mobile HAPs are communicating to each other through an A2A channel with altitudes  $h_1$  and  $h_2$  respectively. Due to the fact that the nature of HAPs allows them to move without any restricted trajectory, for each time iteration ( $t_i$ ), positions of the HAPs are assumed to be unpredictable. In this scenario, due to the severe pathloss that is caused by the short wavelength of the transmitted signal, the 3D distance ( $D_{3D}$ ) between the two HAPs is assumed to be limited and the two dimensional (2D) distance ( $D_{2D}$ ) between them is assumed to change by depending on  $D_{3D}$  along with  $h_1$  and  $h_2$ .

The main purpose of this study is to characterize the A2A channel for beamforming applications in Flying Ad-Hoc Networks (FANETs). Therefore, the carrier frequency ( $f_c$ ) is selected as a mmWave band frequency and each HAP is assumed to be equipped with  $N \times N$  directional Uniform Rectangular Planar Array (URPA) antennas. Due to the fact

<sup>1</sup>*Notations:* Note that vectors are denoted by bold-small letters, matrices are denoted by bold-capital letters, scalar numbers are denoted by non-bold capital letters, and complex numbers or elements indexing are denoted by non-bold small letters based on the context. Also,  $H$  is given to denote the Hermitian transpose a corresponding matrix, whereas  $\otimes$  is the Kronecker product between two matrices, and  $\text{tr}(\cdot)$  is the trace of a matrix.

that the operating frequency is at mmWave band and the beamforming is applied on the transmitted signal, the position vectors of the two HAPs in each time iteration must be accurately identified.

For this reason, a 3D approach is adopted in the proposed channel model and the time varying direction angles of HAP-1 and HAP-2 are assumed to be dependent on both azimuth and elevation domains. The direction angles of HAP-1 in azimuth and elevation domains are given as  $\mathcal{D}_{A_1}$  and  $\mathcal{D}_{E_1}$  respectively, whereas these angles for HAP-2 are provided as  $\mathcal{D}_{A_2}$  and  $\mathcal{D}_{E_2}$ .

Since the movement directions of the HAPs in time are random and independent, the transmitted signal beams from one HAP will not always be guaranteed to be perfectly aligned with the receiver of the other HAP. This is due to the fact that if the antenna directions are considered to be the same as the moving directions of the HAPs, the communication between them will be corrupted for every change in direction. Therefore, in order to provide the continuity of communication between the two HAPs, the steering directions of the antennas located in the HAPs are required to be adjusted by manipulating the phase angles of the antennas in accordance with the direction angles of the HAPs. In this regard, the angles  $(\theta_1, \phi_1)$  are given as the phase angles of HAP-1 in azimuth and elevation domains and  $(\theta_2, \phi_2)$  are given as the phase angles of HAP-2 in azimuth and elevation domains respectively.<sup>2</sup>

### B. Mobility Model

In this study, the Gauss-Markov mobility model [19] is exploited in conjunction with a 3D random walk mobility model [20]. The reason why such a collaborative mobility model is adopted in this study is that even though the Gauss-Markov mobility model is widely used in the literature to demonstrate the temporal relation of the moving objects, in real-life scenarios, the probability of unexpected sudden rotations during the movement of these objects is substantially high and needs to be taken under consideration. Therefore, in this study, a random walk mobility model where the next maneuver of the object varies independently than the previous action is exploited in a harmony with the Gauss-Markov mobility model.

In this regard, for both HAPs, the velocity, azimuth direction, and elevation direction vectors are calculated in each time iteration,  $t_i$ , with respect to the values of these vectors at time instant  $t_{i-1}$  as follows [21]

$$\begin{aligned} \mathcal{V}_{(1,2)}(t_i) &= \alpha_{\mathcal{V}_{(1,2)}} \mathcal{V}_{(1,2)}(t_{i-1}) + \\ & (1 - \alpha_{\mathcal{V}_{(1,2)}}) \mu_{\mathcal{V}_{(1,2)}} + \sqrt{1 - (\alpha_{\mathcal{V}_{(1,2)}})^2} X_{(1,2)i-1}, \end{aligned} \quad (1)$$

$$\begin{aligned} \mathcal{D}_{A(1,2)}(t_i) &= \alpha_{\mathcal{D}_{A(1,2)}} \mathcal{D}_{A(1,2)}(t_{i-1}) + \\ & (1 - \alpha_{\mathcal{D}_{A(1,2)}}) \mu_{\mathcal{D}_{A(1,2)}} + \sqrt{1 - (\alpha_{\mathcal{D}_{A(1,2)}})^2} Y_{(1,2)i-1}, \end{aligned} \quad (2)$$

<sup>2</sup>In Section III, HAP-1 is considered as the transmitter and HAP-2 is considered as the receiver. Therefore, to preserve the flow of the paper and keep the readers understanding high, the notations of  $(\theta_1, \phi_1)$  and  $(\theta_2, \phi_2)$  are changed accordingly in Section III and renoted as  $(\theta_1 = \theta^{Tx}, \phi_1 = \phi^{Tx})$  and  $(\theta_2 = \theta^{Rx}, \phi_2 = \phi^{Rx})$ .

$$\begin{aligned} \mathcal{D}_{E(1,2)}(t_i) &= \alpha_{\mathcal{D}_{E(1,2)}} \mathcal{D}_{E(1,2)}(t_{i-1}) + \\ & (1 - \alpha_{\mathcal{D}_{E(1,2)}}) \mu_{\mathcal{D}_{E(1,2)}} + \sqrt{1 - (\alpha_{\mathcal{D}_{E(1,2)}})^2} Z_{(1,2)i-1}, \end{aligned} \quad (3)$$

where  $i \in \{1, 2, 3, \dots\}$  is the iteration factor that is used to denote each time iteration,  $t_i$ . While  $\mathcal{V}_{(1,2)}(t_i)$ ,  $\mathcal{D}_{A(1,2)}(t_i)$ , and  $\mathcal{D}_{E(1,2)}(t_i)$  are the velocity, azimuth direction, and elevation direction vectors at time instant  $t_i$  for both HAP-1 and HAP-2 respectively,  $\mathcal{V}_{(1,2)}(t_{i-1})$ ,  $\mathcal{D}_{A(1,2)}(t_{i-1})$ ,  $\mathcal{D}_{E(1,2)}(t_{i-1})$  represent the values of these vectors at time instant  $t_{i-1}$ .  $\mu_{\mathcal{V}_{(1,2)}}$ ,  $\mu_{\mathcal{D}_{A(1,2)}}$ , and  $\mu_{\mathcal{D}_{E(1,2)}}$  are given as the asymptotic mean values of velocity, azimuth direction deviation, and elevation direction deviation respectively for both HAP-1 and HAP-2 when  $i$  approaches to infinity. The parameters  $X, Y, Z$  are given as the Gaussian distributed random variables with zero mean and unity variance, whereas the parameters of  $\alpha$ , namely  $\alpha_{\mathcal{V}_{(1,2)}}$ ,  $\alpha_{\mathcal{D}_{A(1,2)}}$ ,  $\alpha_{\mathcal{D}_{E(1,2)}}$  are the tuning parameters of HAP-1 and HAP-2 that have a range between  $[0, 1]$ , which defines the level of randomness and memory [22].

By assigning the initial values of velocity and direction vectors, the formulations of the Gauss-Markov mobility model given in (1), (2), (3) can be rewritten as [7]

$$\begin{aligned} \mathcal{V}_{(1,2)}(t_i) &= (\alpha_{\mathcal{V}_{(1,2)}})^i \mathcal{V}_{(1,2)}(t_0) + \\ & (1 - (\alpha_{\mathcal{V}_{(1,2)}})^i) \mu_{\mathcal{V}_{(1,2)}} + \sqrt{1 - (\alpha_{\mathcal{V}_{(1,2)}})^2} \\ & \sum_{j=0}^{i-1} (\alpha_{\mathcal{V}_{(1,2)}})^{i-j-1} X_j, \end{aligned} \quad (4)$$

$$\begin{aligned} \mathcal{D}_{A(1,2)}(t_i) &= (\alpha_{\mathcal{D}_{A(1,2)}})^i \mathcal{D}_{A(1,2)}(t_0) + \\ & (1 - (\alpha_{\mathcal{D}_{A(1,2)}})^i) \mu_{\mathcal{D}_{A(1,2)}} + \sqrt{1 - (\alpha_{\mathcal{D}_{A(1,2)}})^2} \\ & \sum_{j=0}^{i-1} (\alpha_{\mathcal{D}_{A(1,2)}})^{i-j-1} Y_j, \end{aligned} \quad (5)$$

$$\begin{aligned} \mathcal{D}_{E(1,2)}(t_i) &= (\alpha_{\mathcal{D}_{E(1,2)}})^i \mathcal{D}_{E(1,2)}(t_0) + \\ & (1 - (\alpha_{\mathcal{D}_{E(1,2)}})^i) \mu_{\mathcal{D}_{E(1,2)}} + \sqrt{1 - (\alpha_{\mathcal{D}_{E(1,2)}})^2} \\ & \sum_{j=0}^{i-1} (\alpha_{\mathcal{D}_{E(1,2)}})^{i-j-1} Z_j, \end{aligned} \quad (6)$$

In this study, it is assumed that the movement paths of the HAPs are predefined for a random scenario. Therefore it is expected that there are some sudden rotations during the movement of the HAPs. In order to characterize these sudden rotations, the random walk mobility model is exploited in conjunction with the Gauss-Markov mobility model. Even though the number of sudden rotations and the duration of the predictable motion of the HAPs are randomly selected, it should be noted that the randomness that is mentioned in this mobility model is predefined for the general trajectory. This means that once the trajectory is defined by authorities for a specific scenario, the movement path is restricted to

follow the predefined trajectory. However, unexpected changes in the environment and the mission updates may still force the HAPs to deviate their directions from the predefined trajectory [23]. The clarification of this trajectory definition and the randomness mentioned in this mobility model is crucial due to the fact that allowing HAPs to fly in the air randomly may cause some safety issues, which is not the case proposed in this paper.

Fig. 1 and Fig. 2 show the velocity and direction vectors of HAP-1 and HAP-2 respectively for a 100 seconds time duration when the speed of the HAPs is considered as 100 m/s [24]. As it can be seen from Fig. 1(a) and Fig. 2(a), the variables in the velocity vectors of the two HAPs are almost equal 100 m/s and does not change drastically during the given time period. The reason why is that for the velocity calculations of the HAPs, only the Gauss-Markov model is considered with the tuning parameters  $\alpha_{\mathcal{V}(1,2)} = \{0.5919, 0.3718\}$ . By adopting such a mobility model, it is aimed to keep the velocities of the HAPs constant rather than changing the values of them in each time iteration.

On the other hand, while Fig. 1(b) and Fig. 2(b) show the direction vectors of HAP-1 and HAP-2 respectively in the azimuth domain, the direction vectors of HAP-1 and HAP-2 in the elevation domain are shown in Fig. 1(c) and Fig. 2(c) respectively. It can be observed from these figures that for both azimuth and elevation directions of both HAPs, the Gauss-Markov model is preserved until a certain time duration. However, at a randomly selected time, the direction variables are assigned to an irrelevant value that is independent from the previous time instant. Such a mobility model is applied in this study to illustrate the sudden rotations of the HAPs at an unexpected time instant.

It should be noted that even though the HAPs that are deployed in real-life scenarios are bulky vehicles and their motion in time is mostly predictable, since their nature allows them to operate in the air by following a scenario based trajectory, such a mixture of Gauss-Markov and 3D random walk model reflects the true mobility characteristics of the HAPs better than the Gauss-Markov model alone. In order to illustrate the movement of both HAPs in the air with the joint Gauss-Markov and 3D random walk model, their position change at an altitude  $h_1 \approx h_2 \approx 20$  km in time is given in Fig. 3. In this figure, while the blue points represent the position of HAP-1, the red points represent the position of HAP-2 in each time iteration. As it can be observed from this figure, while both HAPs move in a constant direction for a certain time period, at a random moment, directions of them randomly change, which could be justified by a mission update in a real-life scenario.

### C. Effect of Doppler Caused by Mobility

As stated earlier, in this paper, the communication between two mobile HAPs is considered to be conducted by a signal that operates at mmWave band. Under these conditions, it is expected that the effect of Doppler degrades the quality of communication substantially due to the frequency shift. Therefore, it should be analytically calculated and considered

throughout the rest of the proposed channel model. In this regard, the Doppler frequency in terms of speed, direction, and phase angle is given as [25]

$$f_d(t_i) = \frac{\mathcal{V}_1(t_i)}{\lambda} \left( \cos(\theta_1(t_i) - D_{A_1}(t_i)) \cos(\phi_1) \cos(D_{E_1}(t_i)) + \sin(\phi_1) \sin(D_{E_1}(t_i)) \right) + \frac{\mathcal{V}_2(t_i)}{\lambda} \left( \cos(\theta_2(t_i) - D_{A_2}(t_i)) \cos(\phi_2) \cos(D_{E_2}(t_i)) + \sin(\phi_2) \sin(D_{E_2}(t_i)) \right). \quad (7)$$

Note that the validity of given equation in (7) exists in those cases where the line-of-sight (LoS) condition is satisfied, which means the phase angles of the HAPs are approximated to be  $\theta_1 \approx 0$ ,  $\theta_2 \approx \pi$ , and  $\phi_1 \approx \phi_2 \approx \mathcal{D}_E^{1|2}$  where  $\mathcal{D}_E^{1|2}$  is the elevation angle of HAP-1 relative to HAP-2 and given as

$$\mathcal{D}_E^{1|2} = \tan^{-1} \left( \frac{h_1 - h_2}{D_{2D}} \right). \quad (8)$$

However, since the communication between the two HAPs is in the mmWave frequency, the probability of the causes of deviation such as reflection, refraction, etc. is substantially high, which may result in the LoS to be broken. In such a case, the given equation in (7) has to be adapted to non LoS (NLoS) conditions by defining the Azimuth Angle of Departure (AAOD), Elevation Angle of Departure (EAOD), Azimuth Angle of Arrival (AAOA), and Elevation Angle of Arrival (EAOA) of the local scatterers.

## III. SYSTEM ANALYSIS

In this section, MIMO characteristics of the HAPs are interrogated in terms of beam gain and capacity. In order to operate this interrogation, a signal beam is assumed to be transmitted from the HAP-1 and received by the HAP-2 at a time instant  $t_i$ . The hardware characteristics of the HAPs are considered to be identical where each HAP deploys an URPA that contains  $N \times N$  identical isotropic antennas. Therefore, the number of transmit antennas ( $N_{Tx}$ ) on HAP-1 and the number of receive antennas ( $N_{Rx}$ ) on HAP-2 are considered to be equal and uniformly placed as shown in Fig. 4.

Under these conditions, the received equivalent signal of a specific antenna element where the signal impinges on the antenna with an angle of arrival in azimuth domain (AAOA) and elevation domain (EAOA) can be given as

$$y_{m,n}(t_i) = \sqrt{\rho_{m,n}} h_{m,n}(t_i) \times s \left( t_i - ((n-1)\tau_x + (m-1)\tau_y) \right) + \omega_{m,n}(t_i), \quad (9)$$



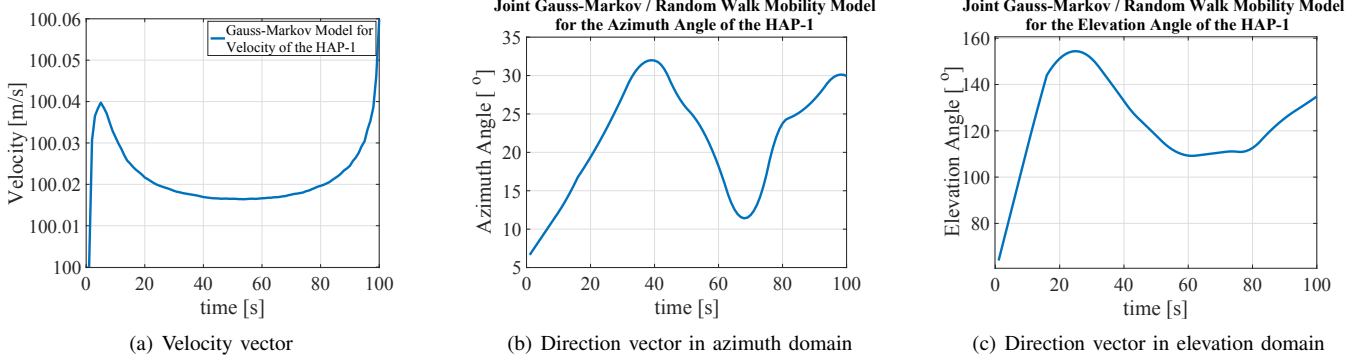


Fig. 1: Position vectors of HAP-1

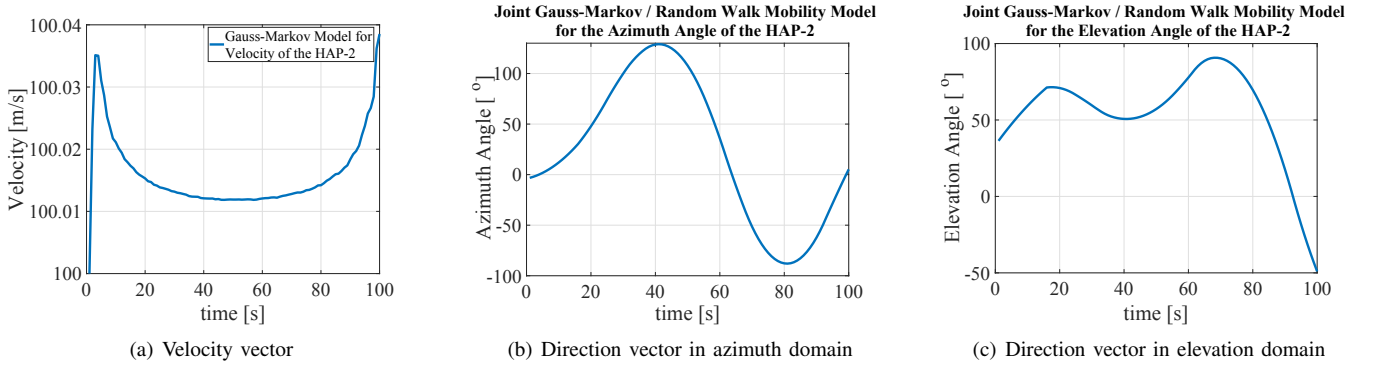


Fig. 2: Position vectors of HAP-2

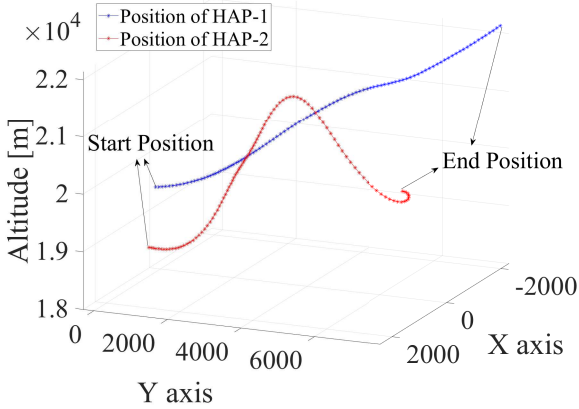


Fig. 3: Positions of HAP-1 and HAP-2 in the air for the given time period

where  $(m, n)$  are the coordination indicators of the antenna array in x-axis and y-axis respectively, and

$$h_{m,n}(t_i) \in \mathbf{H}(t_i) = \begin{bmatrix} h_{1,1}(t_i) & h_{1,2}(t_i) & \cdots & h_{1,n}(t_i) \\ h_{2,1}(t_i) & h_{2,2}(t_i) & \cdots & h_{2,n}(t_i) \\ \vdots & \vdots & \ddots & \vdots \\ h_{m,1}(t_i) & h_{m,2}(t_i) & \cdots & h_{m,n}(t_i) \end{bmatrix} \quad (10)$$

is the complex Rayleigh channel coefficient of the  $(m, n)$ th

antenna,  $s(\cdot)$  is the transmitted symbol, and

$$\tau_x = \frac{d_x \sin \theta^{Rx} \cos \phi^{Rx}}{c}, \quad (11)$$

$$\tau_y = \frac{d_y \sin \theta^{Rx} \sin \phi^{Rx}}{c} \quad (12)$$

are the time delays between the adjacent antennas in x-axis and y-axis respectively with antenna spacing distance  $d_{x,y} = \frac{\lambda_c}{2}$ , and  $\omega_{m,n}(t_i)$  is the additive white Gaussian noise with zero mean and unity variance. Moreover, by exploiting the time delays in x-axis and y-axis together, the maximum time delay between antenna elements at the receiver can be calculated as

$$\tau_{max} = \left| (N_{Rx} - 1) \left( \frac{d_x \sin \theta^{Rx} \cos \phi^{Rx} + d_y \sin \theta^{Rx} \sin \phi^{Rx}}{c} \right) \right|. \quad (13)$$

The representation of the received data can also be given in discrete time by assuming that the amount of Nyquist sampling statistics is adequate. In this case, the regarding representation can be given as

$$y_{m,n}(k) = \sqrt{\rho_{m,n}} \sum_{l=0}^{v-1} h_{m,n}(k, l) \times s(k - ((n-1)l + (m-1)l)) + \omega_{m,n}(k), \quad (14)$$

where  $h_{m,n}(k, l)$  is given as the channel impulse response of the  $l$ -th tap and  $v$  is the limit of iteration to increase the approximation of finite impulse response of the received data.

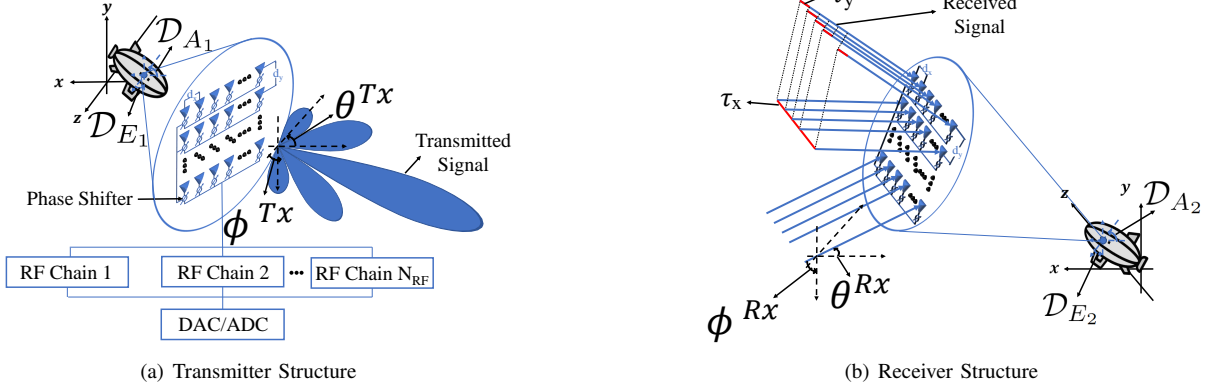


Fig. 4: Transmitter and receiver structures of the proposed scenario

If the Discrete Fourier Transform (DFT) is conducted on (14), the received signal of  $(m, n)$ -th antenna in frequency domain can be calculated as

$$y_{m,n}(f(t_i)) = \mathbf{a}(\theta^{Rx}, \phi^{Rx}, f(t_i))s(f(t_i)) + \omega_{m,n}(f(t_i)), \quad (15)$$

where  $\mathbf{a}(\cdot)$  is the steering vector and given as [26]

$$\mathbf{a}(\theta, \phi, f(t_i)) = \mathbf{v}_x(\theta, \phi, f(t_i)) \otimes \mathbf{v}_y(\theta, \phi, f(t_i)). \quad (16)$$

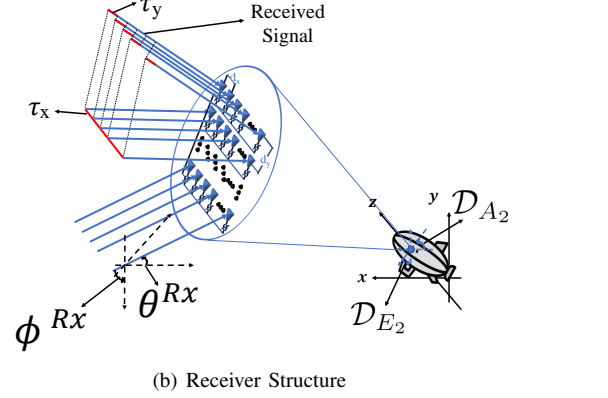
The corresponding expressions for  $\mathbf{v}_x(\cdot)$  and  $\mathbf{v}_y(\cdot)$  are given respectively as

$$\mathbf{v}_x(\theta, \phi, f(t_i)) = \left[ 1, \exp\left(-j2\pi\frac{f(t_i)}{c}d_x \sin\theta \cos\phi\right), \dots, \exp\left(-j(n-1)2\pi\frac{f(t_i)}{c}d_x \sin\theta \cos\phi\right) \right]^T \in \mathbb{C}^{1 \times N_{Tx, Rx-x}}, \quad (17)$$

$$\mathbf{v}_y(\theta, \phi, f(t_i)) = \left[ 1, \exp\left(-j2\pi\frac{f(t_i)}{c}d_y \sin\theta \sin\phi\right), \dots, \exp\left(-j(m-1)2\pi\frac{f(t_i)}{c}d_y \sin\theta \sin\phi\right) \right]^T \in \mathbb{C}^{1 \times N_{Tx, Rx-y}}, \quad (18)$$

where  $N_{Tx, Rx-x}$  are the number of transmit/receive antenna elements in x-axis and  $N_{Tx, Rx-y}$  are the number of transmit/receive antenna elements in y-axis respectively. It should be noted that the steering vector  $\mathbf{a}(\cdot)$  is needed to be calculated for both the transmitter HAP and receiver HAP separately. In this regard, notations for these two HAPs can be given as  $\mathbf{a}_{Tx}(\theta^{Tx}, \phi^{Tx}, f(t_i))$  and  $\mathbf{a}_{Rx}(\theta^{Rx}, \phi^{Rx}, f(t_i))$  respectively.

Due to the Doppler spread and multipath, the channel between the two HAPs is expected to be highly selective in both time and frequency domain, which means the channel matrix  $\mathbf{H}(f(t_i))$  will vary rapidly as the HAPs move in time. In order to characterize the channel, the steering vectors of the transmitter HAP and receiver HAP can be exploited. On this matter, representation of the  $\mathbf{H}(f(t_i))$  for  $K$  scattering clusters and  $L$  propagation paths can be given as [27], [28]



$$\mathbf{H}(f(t_i)) = \frac{N_{Tx}N_{Rx}}{\sqrt{KL}} \sum_{k=1}^K \sum_{l=1}^L g_{kl}(t_i) \Lambda_{Rx}(\theta_{kl}^{Rx}, \phi_{kl}^{Rx}, f(t_i)) \Lambda_{Tx}(\theta_{kl}^{Tx}, \phi_{kl}^{Tx}, f(t_i)) \mathbf{a}_{Rx}(\theta_{kl}^{Rx}, \phi_{kl}^{Rx}, f(t_i)) \mathbf{a}_{Tx}^H(\theta_{kl}^{Tx}, \phi_{kl}^{Tx}, f(t_i)) \exp(j2\pi f_{d_{\max}} t_i \sin\theta_{kl}^{rd} \cos\phi_{kl}^{rd}), \quad (19)$$

where  $g_{kl}$  is the randomly distributed complex Gaussian small-scale gain of the corresponding  $l$ -th path of the  $k$ -th cluster with zero mean and unity variance,  $\theta_{kl}^{Tx}$ ,  $\phi_{kl}^{Tx}$ , and  $\theta_{kl}^{Rx}$ ,  $\phi_{kl}^{Rx}$  are the AAOD, EAOD, and AAOA, EAOA of the  $l$ -th path of the  $k$ -th cluster respectively,  $\Lambda_{Tx}(\theta_{kl}^{Tx}, \phi_{kl}^{Tx}, f(t_i))$  and  $\Lambda_{Rx}(\theta_{kl}^{Rx}, \phi_{kl}^{Rx}, f(t_i))$  are the antenna gain for each element of the transmitter and receiver respectively, which are assumed to be  $\Lambda_{Tx}(\theta_{kl}^{Tx}, \phi_{kl}^{Tx}, f(t_i)) = \Lambda_{Rx}(\theta_{kl}^{Rx}, \phi_{kl}^{Rx}, f(t_i)) = 1$ .

The exponential part in (19) is usually considered to be 1 in those cases where the mobility of HAPs is not considered. However, since in this scenario the mobility plays a crucial role to characterize the channel, the Doppler frequency creates a necessity to consider its maximum value,  $f_{d_{\max}}$ , in the representation of the channel. It also should be mentioned that the angles  $\theta_{kl}^{rd}$  and  $\phi_{kl}^{rd}$  used in the exponential part to represent the AAOA and EAOA are relative to the direction of motion of the receiver HAP, which were given in Section II-B as  $\mathcal{D}_{A_2}$  and  $\mathcal{D}_{E_2}$  for azimuth and elevation domains respectively.

#### A. Beam Gain

Due to the fact that the transmitted data is in shape of a narrow beam, the alignment of the signal in accordance with the exact position of the receiver is crucial. In those cases where the beam alignment is not operated successfully, the performance of the communication might either degrade dramatically or get completely lost depending on the severeness of the misalignment of the beam. In MIMO systems, the beam alignment is achieved by deploying phase shifters for each analog antenna element to focus the signal on the receiver with a specific angle as shown in Fig. 4. Even though such an alignment can be applicable on stationary access points, the unpredictable movement of the HAPs in the proposed scenario creates a challenge to adapt the phase shifters to a different

focus angle momentarily. Therefore in this section, the effect of beam misalignment is interrogated.

In this regard, the focus angles of the beam at the transmission side is defined as  $\theta_F^{Rx}$  and  $\phi_F^{Rx}$  in the azimuth and elevation domains respectively. The analog beamforming matrix for UPA is denoted as

$$\mathbf{W} = \left[ \mathbf{w}_1, \mathbf{w}_2, \dots, \mathbf{w}_{N_{RF}} \right] \in \mathbb{C}^{N_{Tx} N_{Rx} \times N_{RF}}, \quad (20)$$

where  $N_{RF}$  is the number of RF chains at the transmitter and  $\mathbf{w} \in \mathbb{C}^{N_{Tx} \times N_{Rx}}$  is the beamforming vector of the corresponding RF chain.

The calculation of the vector  $\mathbf{w}$  for each RF chain can be calculated as follows

$$\mathbf{w} = \mathbf{w}_x \otimes \mathbf{w}_y. \quad (21)$$

The corresponding expressions for  $\mathbf{w}_x(\cdot)$  and  $\mathbf{w}_y(\cdot)$  are given respectively as

$$\mathbf{w}_x = [e^{-j\beta_{1x}}, e^{-j\beta_{2x}}, \dots, e^{-j\beta_{n_x}}] \in \mathbb{C}^{1 \times N_{Tx-x}}, \quad (22)$$

$$\mathbf{w}_y = [e^{-j\beta_{1y}}, e^{-j\beta_{2y}}, \dots, e^{-j\beta_{m_y}}] \in \mathbb{C}^{1 \times N_{Tx-y}}, \quad (23)$$

where

$$\beta_{n_x} = \frac{2\pi}{\lambda_c} (n-1) d_x \sin \theta^{Tx} \cos \phi^{Tx}, \quad (24)$$

$$\beta_{m_y} = \frac{2\pi}{\lambda_c} (m-1) d_y \sin \theta^{Tx} \sin \phi^{Tx} \quad (25)$$

are the phase shifters of the  $(m, n)$ -th antenna element.

By utilizing the beamforming matrix  $\mathbf{W}$  and the steering vector of the receiver  $\mathbf{a}_{\mathbf{R}\mathbf{x}}(\theta^{Rx}, \phi^{Rx}, f(t_i))$ , the beam gain can be calculated as follows<sup>3</sup>

$$\begin{aligned} g(\mathbf{W}, \theta^{Rx}, \phi^{Rx}, f(t_i)) &= \mathbf{W}^H \mathbf{a}_{\mathbf{R}\mathbf{x}}(\theta^{Rx}, \phi^{Rx}, f(t_i)) \\ &= \sum_{n=1}^{N_{Tx-x}} \sum_{m=1}^{N_{Tx-y}} e^{-j2\pi(n-1)\frac{d_x}{c}\mu_x} \otimes e^{-j2\pi(m-1)\frac{d_y}{c}\mu_y}, \end{aligned} \quad (26)$$

which can be further expressed as

$$\begin{aligned} g(\mu_x, \mu_y, t_i) &= \frac{\sin(-N_{Tx}\pi\frac{d_x}{c}\mu_x)}{\sin(-\pi\frac{d_x}{c}\mu_x)} e^{-2j\pi\frac{d_x}{c}(N_{Tx}-1)\mu_x} \otimes \\ &\frac{\sin(-N_{Tx}\pi\frac{d_y}{c}\mu_y)}{\sin(-\pi\frac{d_y}{c}\mu_y)} e^{-2j\pi\frac{d_y}{c}(N_{Tx}-1)\mu_y}, \end{aligned} \quad (27)$$

where

$$\mu_x = (f_c(t_i) + f_d(t_i)) \sin \theta^{Rx} - f_c(t_i) \sin \theta_F^{Rx}, \quad (28)$$

$$\mu_y = (f_c(t_i) + f_d(t_i)) \sin \phi^{Rx} - f_c(t_i) \sin \phi_F^{Rx}. \quad (29)$$

The maximum achievable gain can be obtained as  $g_{\max} = g(0, 0, t_i) = N_{Tx}$  in the case where  $\mu_x = \mu_y = 0$ , which means the effect of Doppler does not exist and the focus angles in both azimuth and elevation domains that are required to impinging the transmitted signal upon the receiver are equal to the

arrival angles of the beam. In this case, the effective channel between the transmitter and receiver can be interpreted to be the multiplication of the analog beamforming matrix and the steering vector of the receiver, which can be mathematically expressed as

$$h_{eff} = g(\mathbf{W}, \theta^{Rx}, \phi^{Rx}, f(t_i)) = \mathbf{W}^H \mathbf{a}_{\mathbf{R}\mathbf{x}}(\theta^{Rx}, \phi^{Rx}, f(t_i)). \quad (30)$$

However, when the effect of Doppler is included, the matching possibility of the arrival angles and the focus angles decreases dramatically due to the dispersion in angular domain, which causes the focus angles to get shifted from their desired values. In such a case, the phase shifting is required to be operated in such a way that the analog beamforming matrix can compensate the effect of the beam-selective channel.

The illustration of the beam gain at a time instant  $t_i$  is given in Fig. 5 for  $N_{Tx} = 16$  and  $(\theta_F^{Rx}, \phi_F^{Rx}) = (60^\circ, 30^\circ)$ . As it can be seen from this figure, in the case where the Doppler doesn't exist, the beam gain reaches its maximum value  $N_{Tx}$  when the direction angles of the arriving beam  $(\theta^{Rx}, \phi^{Rx})$  are equal to the selected focus angles  $(\theta_F^{Rx}, \phi_F^{Rx})$  and gradually degrades as the difference between  $(\theta^{Rx}, \phi^{Rx})$  and  $(\theta_F^{Rx}, \phi_F^{Rx})$  gets larger. However, when the Doppler is included, the focus angles are shifted and the maximum gain is not achieved on the desired values.

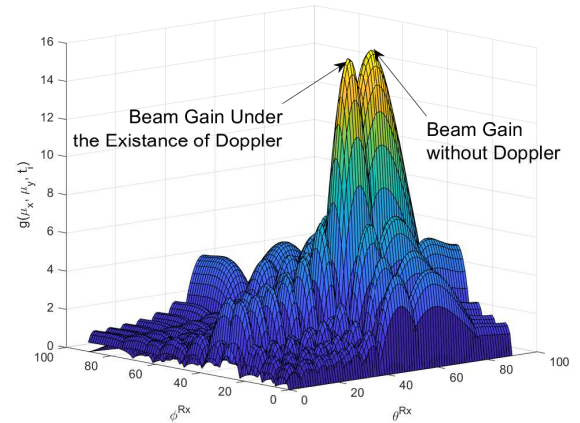


Fig. 5: Beam gain for  $N_{Tx} = 16$ , and  $(\theta_F^{Rx}, \phi_F^{Rx}) = (60^\circ, 30^\circ)$

## B. System Capacity

Due to the high mobility of the HAPs in the proposed scenario, it is expected that the Doppler spread causes the channel to be highly selective in time domain and multipath causes the channel to be highly selective in frequency domain. In order to compensate the effects of the frequency-selective channel, it's assumed that a Cyclic Prefix (CP) that is longer than the time delay is utilized in time domain to avoid Inter-Symbol Interference (ISI). Therefore, the calculations of the system capacity is conducted by considering only the existence of time-selective channel. Under the existence of such a time-selective channel, when a multicarrier waveform is utilized rather than a single-carrier waveform, the resulting interference between the carriers has the potential to decrease

<sup>3</sup>Note that the transmitter gain can also be obtained by exploiting (26) by changing the indicator "Rx" to "Tx"

the performance of the communication due to the fact that the orthogonality between these carriers is corrupted. In order to evaluate the effect of the interference between these carriers, namely Inter-Carrier Interference (ICI), upon the multicarrier communication between the two mobile HAPs, this section analyses the signal-to-interference-plus-noise ratio (SINR) performance of the proposed scenario.

In this manner, the received signal of  $(m, n)$ -th antenna calculated in (14) can be transformed into

$$\begin{aligned} y_{m,n}(p_{N_c}, f(t_i)) &= \sqrt{\rho_{m,n}} \left( h_{m,n}(p_{N_c}, f(t_i)) \times \right. \\ & s(p_{N_c}, t_i - ((n-1)\tau_x + (m-1)\tau_y)) + \\ & \sum_{\substack{q=0 \\ q \neq p}}^{N_c-1} h_{m,n}(q, f(t_i)) \times \\ & \left. s(q, t_i - ((n-1)\tau_x + (m-1)\tau_y)) \right) + \omega_{m,n}(p, t_i), \end{aligned} \quad (31)$$

where  $N_c$  is the number of carriers in each antenna element,  $p \in \{0, 1, \dots, N_c - 1\}$  is the specific carrier of the  $(m, n)$ -th antenna element that the data is received from, and  $q \in \{0, 1, \dots, N_c - 1\}$ ,  $q \neq p$  is all the rest of the carriers except  $p$  that are considered as noise due to the ICI. In order to take (31) one step further, the case where the spatial diversity is exploited can be considered. In such a case the received signal formula evolves into

$$\begin{aligned} \mathbf{y}_{m,n}(f(t_i)) &= \sqrt{\rho_{m,n}} \left( \left[ h_{m,n}(p_1, p_1, f(t_i)) \times s(p_1, t_i - \right. \right. \\ & \left. \left. ((n-1)\tau_x + (m-1)\tau_y) \right), \dots, h_{m,n}(p_{N_c}, p_{N_c}, f(t_i)) \times \right. \\ & \left. s(p_{N_c}, t_i - ((n-1)\tau_x + (m-1)\tau_y)) \right] + \\ & \sum_{\substack{q=0 \\ q \neq p}}^{N_c-1} h_{m,n}(p, q, f(t_i)) \times s(q, t_i - ((n-1)\tau_x + (m-1)\tau_y)) \Big) \\ & + \omega_{m,n}(p_{N_c}, t_i) \in \mathbb{C}^{1 \times N_c}, \end{aligned} \quad (32)$$

where

$$\mathbf{h}_{m,n}(p_{N_c}, f(t_i)) \in [h_{m,n}(p_1, f(t_i)), \dots, h_{m,n}(p_{N_c}, f(t_i))], \quad \mathbb{C}^{1 \times N_c} \quad (33)$$

is the channel vector of the  $(m, n)$ -th antenna element that consists of the channel coefficients of each carrier  $h_{m,n}(p_{N_c}, f(t_i))$ . For the sake of simplification, (32) can be reformed as

$$\begin{aligned} \mathbf{y}_{m,n}(f(t_i)) &= \sqrt{\rho_{m,n}} \left( \mathbf{h}_{m,n}(p_{N_c}, p_{N_c}, f(t_i)) \times \right. \\ & \mathbf{x}(p_{N_c}, t_i - ((n-1)\tau_x + (m-1)\tau_y)) + \sum_{\substack{q=0 \\ q \neq p}}^{N_c-1} \mathbf{h}_{m,n}(p, q, f(t_i)) \\ & \left. \mathbf{x}(q, t_i - ((n-1)\tau_x + (m-1)\tau_y)) \right) + \omega_{m,n}(p_{N_c}, t_i) \in \mathbb{C}^{1 \times N_c}. \end{aligned} \quad (34)$$

In this case, the received signal at time instant  $t_i$  can be expressed in vector form as

$$\begin{aligned} \mathbf{Y}(f(t_i)) &= [\mathbf{y}_{1,1}(f(t_i)), \mathbf{y}_{1,2}(f(t_i)), \dots, \mathbf{y}_{1,n}(f(t_i)), \\ & \mathbf{y}_{2,1}(f(t_i)), \mathbf{y}_{2,2}(f(t_i)), \dots, \mathbf{y}_{2,n}(f(t_i)), \dots, \\ & \mathbf{y}_{m,1}(f(t_i)), \mathbf{y}_{m,2}(f(t_i)), \dots, \mathbf{y}_{m,n}(f(t_i))], \\ & \in \mathbb{C}^{mn \times N_c}, \end{aligned} \quad (35)$$

and in closed form as

$$\mathbf{Y}(f(t_i)) = \mathbf{H}(p, p, f(t_i)) \mathbf{X}(p) + \sum_{\substack{q=0 \\ q \neq p}}^{N_c-1} \mathbf{H}(p, q, f(t_i)) \mathbf{X}(q) + \omega(p). \quad (36)$$

The ICI analysis of the proposed multicarrier HAP communication can be based upon (36) by calculating the covariance matrix of the total noise  $\hat{\omega}(p) = \omega_{\text{ICI}}(p) + \omega(p)$  where

$$\omega_{\text{ICI}}(q) = \sum_{\substack{q=0 \\ q \neq p}}^{N_c-1} \mathbf{H}(p, q, f(t_i)) \mathbf{X}(q). \quad (37)$$

The procedure to mathematically express the covariance of  $\omega_{\text{ICI}}(p)$  can be represented as

$$\begin{aligned} \mathbb{E} [\omega_{\text{ICI}}(q) \omega_{\text{ICI}}^H(q)] &= \\ \mathbb{E} \left[ \sum_{\substack{p=0 \\ q \neq j}}^{N_c-1} \sum_{\substack{q=0 \\ q \neq j}}^{N_c-1} \mathbf{H}(j, p, f(t_i)) \mathbf{X}(p) \mathbf{X}^H(q) \mathbf{H}^H(j, q, f(t_i)) \right] \\ &= \sum_{\substack{p=0 \\ q \neq j}}^{N_c-1} \sum_{\substack{q=0 \\ q \neq j}}^{N_c-1} \mathbb{E} [\mathbf{H}(j, p, f(t_i)) \mathbf{R}_{XX}(p, q) \mathbf{H}^H(j, q, f(t_i))], \end{aligned} \quad (38)$$

where  $\mathbf{R}_{XX}(p, q)$  is defined to represent the term  $\mathbb{E} [\mathbf{X}(p) \mathbf{X}^H(q)]$ .

The following analysis are composed on the term  $\mathbb{E} [\mathbf{H}(j, p, f(t_i)) \mathbf{R}_{XX}(p, q) \mathbf{H}^H(j, q, f(t_i))]$  given in (38) for the sake of simplicity. In this regard, we start our analysis with the eigendecomposition of the signal covariance matrix given as [29]

$$\mathbf{R}_{XX}(p, q) = \mathbf{U}(p, q) \mathbf{\Lambda}_X(p, q) \mathbf{U}^H(p, q), \quad (39)$$

where  $\mathbf{U}(p, q)$  is the unitary matrix that contain the eigenvectors and

$$\mathbf{\Lambda}_X(p, q) = \text{diag}(\lambda_1(p, q), \dots, \lambda_{N_{Tx}}(p, q)) \quad (40)$$

is the diagonal matrix of the eigenvalues of  $\mathbf{R}_{XX}(p, q)$ . In the conducted analysis, it is assumed that the channel matrix  $\mathbf{H}(j, p, f(t_i))$  consists of independent and identically distributed Gaussian variables. Therefore, it can be stated that the distribution of  $\mathbf{H}(j, p, f(t_i))$  is equivalent to  $\mathbf{H}(j, p, f(t_i)) \mathbf{U}(p, q)$ . In this case, the term  $\mathbb{E} [\mathbf{H}(j, p) \mathbf{R}_{XX}(p, q) \mathbf{H}^H(j, q, f(t_i))]$  can be reformed as

$$\begin{aligned} \mathbb{E} [\mathbf{H}(j, p, f(t_i)) \mathbf{R}_{XX}(p, q) \mathbf{H}^H(j, q, f(t_i))] &= \\ \mathbb{E} [\mathbf{H}(j, p, f(t_i)) \mathbf{\Lambda}_X(p, q) \mathbf{H}^H(j, q, f(t_i))] &. \end{aligned} \quad (41)$$



The investigation of the matrix given in (41) can be conducted more thoroughly by choosing some specific indices. In this regard, the matrix can be represented for the  $(r, s)$ -th element as

$$\begin{aligned} & \{\mathbb{E} [\mathbf{H}(j, p, f(t_i)) \mathbf{\Lambda}_X(p, q) \mathbf{H}^H(j, q, f(t_i))]\}_{r,s} = \\ & \sum_{k=1}^{N_{Tx}} \lambda_k(p, q) \mathbb{E} [\{\mathbf{H}(j, p, f(t_i))\}_{r,k} \{\mathbf{H}^H(j, q, f(t_i))\}_{k,s}] = \\ & \sum_{k=1}^{N_{Tx}} \lambda_k(p, q) \mathbb{E} [\{\mathbf{H}(j, p, f(t_i))\}_{r,k} \{\mathbf{H}^H(j, q, f(t_i))\}_{k,r}] \delta_{r-s}, \end{aligned} \quad (42)$$

where  $\delta_{r-s}$  is the correlation parameter of the matrix.

Note that the final form of (42) is only valid for the case where the channel is uncorrelated, which means that when  $r \neq s$ , the cross-correlation between these values becomes zero and leads the (42) to have a non-zero value. In the case where  $r = s$  the auto-correlation becomes maximum and leads the (42) to become zero.

By using the Fourier basis, (42) can be represented as

$$\begin{aligned} & \mathbb{E} [\{\mathbf{H}(j, p, f(t_i))\}_{r,k} \{\mathbf{H}^H(j, q, f(t_i))\}_{k,r}] = \\ & \frac{1}{N_c^2} \left( \sum_{l=0}^{v-1} \exp(-j2\pi l(p-q)/N_c) \right) \times \\ & \sum_{r_1=0}^{N_c-1} \sum_{r_2=0}^{N_c-1} \mathbb{E} [h_{m,n}^{(k,r)}(r_1, l) h_{m,n}^{(k,r)}(r_2, l)] \times \\ & \exp(j2\pi r_1(p-j)/N_c) \exp(-j2\pi r_2(q-j)/N_c). \end{aligned} \quad (43)$$

As a result, the covariance matrix of the ICI can be given as

$$\begin{aligned} & \mathbb{E} [\omega_{\text{ICI}}(q) \omega_{\text{ICI}}^H(q)] = \\ & \sum_{p=0}^{N_c-1} \sum_{\substack{q=0 \\ q \neq j}}^{N_c-1} \frac{\text{tr}(\mathbf{\Lambda}_X(p, q))}{N_c^2} \left( \sum_{l=0}^{v-1} \exp(-j2\pi l(p-q)/N_c) \right) \times \\ & \left( \sum_{r_1=0}^{N_c-1} \sum_{r_2=0}^{N_c-1} \mathbb{E} [h_{m,n}^{(k,r)}(r_1, l) h_{m,n}^{(k,r)}(r_2, l)] \right) \\ & \exp(j2\pi r_1(p-j)/N_c) \exp(-j2\pi r_2(q-j)/N_c). \end{aligned} \quad (44)$$

After obtaining the covariance matrix of ICI, the calculation of SINR at the  $p$ -th carrier where  $1 \leq p \leq N_c$  can be operated as follows

$$\gamma_p = \frac{E_{x,p} |\mathbf{H}(p, p, f(t_i))|^2}{\sum_{q \neq p} E_{x,q} |\mathbf{H}(p, q, f(t_i))|^2 + E_{x,\omega} |\omega(t_i)|^2}, \quad (45)$$

where  $E_{x,p}$  is the input energy that is allocated to the  $p$ -th carrier and  $E_{x,q}$  is the leakage energy from the  $q$ th carrier that contaminates the  $p$ -th carrier.

Since the analysis of SINR is achieved, now the ergodic capacity of the system can be calculated as follows

$$C = \sum_{p=1}^{N_c} \log_2(1 + \gamma_p). \quad (46)$$

#### IV. PDF OF THE SIGNAL TO INTERFERENCE PLUS NOISE RATIO

In this section, the analytical derivation of the Probability Density Function (PDF) for the proposed channel model's SINR is presented. In this regard, the beam gain given in (27) is approximated for more traceability as follows [30]

$$g(\theta^{Rx}, \phi^{Rx}) = \cos^2 \left( \frac{\pi N_{Tx-x} \theta^{Rx}}{2} \right) \otimes \cos^2 \left( \frac{\pi N_{Tx-y} \phi^{Rx}}{2} \right). \quad (47)$$

Note that the given formulation of  $g(\theta^{Rx}, \phi^{Rx})$  is valid only in the case where the  $|\theta^{Rx}| \leq \frac{1}{N_{Tx-x}}$ , and  $|\phi^{Rx}| \leq \frac{1}{N_{Tx-y}}$ . If these conditions are not satisfied, the beam gain is considered to be 0.

To further simplify the beam gain formulation, (47) can be rewritten as follows

$$\begin{aligned} & g(\theta^{Rx}, \phi^{Rx}) \simeq N_{Tx-x} \Pi(N_{Tx-x} \theta^{Rx}) + \\ & N_{Tx-y} \Pi(N_{Tx-y} \phi^{Rx}) + \\ & N_{Tx} \cos^2 \left( \frac{\pi N_{Tx-x}}{2} \right) \cos^2 \left( \frac{\pi N_{Tx-y}}{2} \right) \times \\ & \Pi(N_{Tx-x} |\theta^{Rx}|) \times \Pi(N_{Tx-y} |\phi^{Rx}|), \end{aligned} \quad (48)$$

where  $\Pi(\cdot) = \begin{cases} 1 & \text{for } |\cdot| \leq 1 \\ 0 & \text{for } |\cdot| > 1 \end{cases}$ . By referring the fact that the  $\{\theta^{Rx}, \phi^{Rx}\}$  are Gaussian distributed, the PDF of the  $g(\theta^{Rx}, \phi^{Rx})$  can be given as

$$\begin{aligned} & f_{g(\theta^{Rx}, \phi^{Rx})}(g(\theta^{Rx}, \phi^{Rx})) = A_{Rx}(\theta^{Rx'}, \phi^{Rx'}) \times \\ & \delta \left( g(\theta^{Rx}, \phi^{Rx}) - N_{Tx} \cos^2 \left( \frac{\pi N_{Tx-x}}{2} \right) \cos^2 \left( \frac{\pi N_{Tx-y}}{2} \right) \right), \end{aligned} \quad (49)$$

where  $\delta(\cdot)$  is the Dirac delta function and  $A_{Rx}$  is the derivation variable given as

$$\begin{aligned} & A_{Rx}(\theta^{Rx'}, \phi^{Rx'}) = Q \left( \frac{N_{Tx} \theta^{Rx'}}{N_{Tx} \phi^{Rx'}} \right) - \\ & \left( Q \left( \frac{1 + N_{Tx} \theta^{Rx'}}{N_{Tx} \phi^{Rx'}} \right) + Q \left( \frac{1 - N_{Tx} \theta^{Rx'}}{N_{Tx} \phi^{Rx'}} \right) \right), \end{aligned} \quad (50)$$

by exploiting the  $Q$ -function,  $Q(\cdot)$ .

Referring to (26), the instantaneous directivity gain of the proposed model can be given as

$$\begin{aligned} & \mathbb{G}(\theta^{Tx/Rx}, \phi^{Tx/Rx}) = g(\mathbf{W}, \theta^{Tx}, \phi^{Tx}, f(t_i)) \\ & g(\mathbf{W}, \theta^{Rx}, \phi^{Rx}, f(t_i)). \end{aligned} \quad (51)$$

By exploiting (49) and (51), the PDF of directivity gain conditioned on the receiver array gain can be given as

$$\begin{aligned} & f_{\mathbb{G}|g(\theta^{Rx}, \phi^{Rx})}(\mathbb{G}) = \frac{A_{Tx}(\theta^{Tx'}, \phi^{Tx'})}{g(\theta^{Rx}, \phi^{Rx})} \times \\ & \delta \left( \frac{\mathbb{G}}{g(\theta^{Rx}, \phi^{Rx})} - N_{Tx} \cos^2 \left( \frac{\pi N_{Tx-x}}{2} \right) \cos^2 \left( \frac{\pi N_{Tx-y}}{2} \right) \right). \end{aligned} \quad (52)$$

From (49) and (52), derivation of the PDF for the directivity gain  $\mathbb{G}$  is given as follows

$$\begin{aligned}
f_{\mathbb{G}}(\mathbb{G}) &= \int f_{\mathbb{G}|g(\theta^{Rx}, \phi^{Rx})}(\mathbb{G}) \times \\
& f_{g(\theta^{Rx}, \phi^{Rx})}(g(\theta^{Rx}, \phi^{Rx})) dg(\theta^{Rx}, \phi^{Rx}) = \\
& \int \frac{A_{Rx}(\theta^{Rx'}, \phi^{Rx}) A_{Tx}(\theta^{Tx'}, \phi^{Tx})}{g(\theta^{Rx}, \phi^{Rx})} \times \\
& \delta\left(g(\theta^{Rx}, \phi^{Rx}) - N_{Tx} \cos^2\left(\frac{\pi N_{Tx-x}}{2}\right) \cos^2\left(\frac{\pi N_{Tx-y}}{2}\right)\right) \\
& \delta\left(\frac{\mathbb{G}}{g(\theta^{Rx}, \phi^{Rx})} - N_{Tx} \cos^2\left(\frac{\pi N_{Tx-x}}{2}\right) \cos^2\left(\frac{\pi N_{Tx-y}}{2}\right)\right) \\
& dg(\theta^{Rx}, \phi^{Rx}), \tag{53}
\end{aligned}$$

$$f_{\mathbb{G}}(\mathbb{G}) = \frac{A_{Rx}(\theta^{Rx'}, \phi^{Rx}) A_{Tx}(\theta^{Tx'}, \phi^{Tx})}{\kappa(N_{Tx-x}, N_{Tx-y})} \times \tag{54}$$

$$\delta(\mathbb{G} - \kappa(N_{Tx-x}, N_{Tx-y})),$$

where

$$\kappa(N_{Tx-x}, N_{Tx-y}) = N_{Tx}^2 \cos^4\left(\frac{\pi N_{Tx-x}}{2}\right) \cos^4\left(\frac{\pi N_{Tx-y}}{2}\right). \tag{55}$$

Now, let us define a Nakagami random variable notated as  $\mathfrak{r}$  and  $\zeta = \mathfrak{r}^2$ . Then, the normalized Gamma random variable can be given as

$$f_{\zeta}(\zeta) = \frac{(m\zeta)^m}{\Gamma(m)} \exp(-m\zeta), \quad \zeta > 0 \tag{56}$$

where  $m$  is the Nakagami fading parameter and  $\Gamma(\cdot)$  is the Gamma function [31].

By using the two equations given in (54) and (56), and using the equation (45) by omitting its ICI variable  $E_{x,q}|\mathbf{H}(p, q, f(t_i))|^2$ , the final form of the random variable SNR can be derived as

$$f_{\gamma_p}(\gamma_p) = \int_0^\infty \frac{E_{x,\omega}|\omega(t_i)|}{\zeta} f_{\mathbb{G}}\left(\frac{E_{x,\omega}|\omega(t_i)|}{\zeta}\right) f_{\zeta}(\zeta) d\zeta, \tag{57}$$

$$\begin{aligned}
f_{\mathbb{G}}\left(\frac{E_{x,\omega}|\omega(t_i)|}{\zeta}\right) &= \\
& \frac{A_{Rx}(\theta^{Rx'}, \phi^{Rx}) A_{Tx}(\theta^{Tx'}, \phi^{Tx})}{\kappa(N_{Tx-x}, N_{Tx-y})} \times \\
& \delta\left(\frac{E_{x,\omega}|\omega(t_i)|}{\zeta} - \kappa(N_{Tx-x}, N_{Tx-y})\right), \tag{58}
\end{aligned}$$

$$f_{\gamma_p}(\gamma_p) = \frac{A_{Rx}(\theta^{Rx'}, \phi^{Rx}) A_{Tx}(\theta^{Tx'}, \phi^{Tx}) m^m}{\gamma_p \Gamma(m)} \times \tag{59}$$

$$\int_0^\infty \zeta^m \exp(-m\zeta) d\zeta,$$

$$f_{\gamma_p}(\gamma_p) = \frac{A_{Rx}(\theta^{Rx'}, \phi^{Rx}) A_{Tx}(\theta^{Tx'}, \phi^{Tx}) m^m}{\gamma_p \Gamma(m)} \times \tag{60}$$

$$\frac{E_{x,\omega}|\omega(t_i)|^m \gamma_p^m}{\kappa(N_{Tx-x}, N_{Tx-y})^m} \exp\left(\frac{-m E_{x,\omega}|\omega(t_i)| \gamma_p}{\kappa(N_{Tx-x}, N_{Tx-y})}\right),$$

$$\begin{aligned}
f_{\gamma_p}(\gamma_p) &= \frac{(E_{x,\omega}|\omega(t_i)| m)^m}{\Gamma(m)} \times \\
& \frac{A_{Rx}(\theta^{Rx'}, \phi^{Rx}) A_{Tx}(\theta^{Tx'}, \phi^{Tx})}{\kappa(N_{Tx-x}, N_{Tx-y})^m} \gamma_p^{m-1} \times \\
& \exp\left(\frac{-m E_{x,\omega}|\omega(t_i)| \gamma_p}{\kappa(N_{Tx-x}, N_{Tx-y})}\right). \tag{61}
\end{aligned}$$

Now the effect of the ICI can be included in the analysis to find the distribution of the SINR. By referring the (45), and (61) the PDF of the ICI for the  $q \in \{0, 1, \dots, N_c - 1\}$ ,  $q \neq p$  can be derived as

$$\begin{aligned}
f_{\gamma_q}(\gamma_q) &= \sum_{q=0}^{N_c-1} \frac{(E_{x,\omega}|\omega(t_i)| m)^m}{\Gamma(m)} \times \\
& \frac{A_{Rx}(\theta^{Rx'}, \phi^{Rx}) A_{Tx}(\theta^{Tx'}, \phi^{Tx})}{\kappa(N_{Tx-x}, N_{Tx-y})^m} \gamma_q^{m-1} \times \\
& \exp\left(\frac{-m E_{x,\omega}|\omega(t_i)| \gamma_q}{\kappa(N_{Tx-x}, N_{Tx-y})}\right). \tag{62}
\end{aligned}$$

Now, if a random noise due to ICI,  $\omega_{ICI}$ , is appended on the Additive White Gaussian Noise (AWGN),  $\omega(t_i)$ , the resulting noise,  $\hat{\omega}(t_i)$ , can be substituted in (63) instead of  $\omega(t_i)$  to include the effect of ICI into the transmitted signal given as

$$\begin{aligned}
f_{\hat{\gamma}_p}(\hat{\gamma}_p) &= \frac{(E_{x,\omega}|\hat{\omega}(t_i)| m)^m}{\Gamma(m)} \times \\
& \frac{A_{Rx}(\theta^{Rx'}, \phi^{Rx}) A_{Tx}(\theta^{Tx'}, \phi^{Tx})}{\kappa(N_{Tx-x}, N_{Tx-y})^m} \hat{\gamma}_p^{m-1} \times \\
& \exp\left(\frac{-m E_{x,\omega}|\hat{\omega}(t_i)| \hat{\gamma}_p}{\kappa(N_{Tx-x}, N_{Tx-y})}\right). \tag{63}
\end{aligned}$$

After completing this step the final form of the distribution of SINR can be given as

$$f_{\gamma}(\gamma) = \int_0^\infty f_{\hat{\gamma}_p}(\hat{\gamma}_p) f_{\gamma_q}(\gamma_q) dp. \tag{64}$$

## V. SIMULATION RESULTS AND DISCUSSION

In this section, the simulation results of the analyzed channel model is presented in terms of SINR, capacity and PDF of SINR. The parameters used in the simulations are given in Table I.

In Fig. 6, the SNR vs. SINR performance is exhibited for different AAOAs and EAOAs by assuming the HAPs are stationary. In this regard, the figure shows the SINR performance in the case where the AAOA and EAOA of the received signal match with the receiver's focus angle. It also shows the cases where the AAOAs and EAOAs of the received signal mismatch with different angles of deviation. It is obvious from the figure that when the AAOAs and EAOAs are matched with the focus angles of the receiver, the performance of SINR is maximized due to the fact that the directivity gain become maximum. However, when the received signal's direction is deviated from the focus angle

TABLE I: Simulation Parameters [32]–[36]

Altitudes of HAP-1 and HAP-2 ( $h_1, h_2$ )	$\approx 20$ km
3D distance between HAP-1 and HAP-2 ( $D_{3D}$ )	$\leq 500$ m
Number of transmit antennas on HAP-1 ( $N_{Tx}$ )	16, 32, 64
Number of receive antennas on HAP-2 ( $N_{Rx}$ )	16, 32, 64
Carrier Frequency ( $f_c$ )	60 GHz
Number of Carriers ( $N_c$ )	4
Number of Taps	4
Direction angles in azimuth domain ( $\mathcal{D}_{A(1,2)}$ )	$[-\pi, \pi]$
Direction angles in elevation domain ( $\mathcal{D}_{E(1,2)}$ )	$[-\pi, \pi]$
Phase angles in azimuth domain ( $\theta_{1,2} = \theta^{Tx,Rx}$ )	$[-\pi, \pi]$
Phase angles in elevation domain ( $\phi_{1,2} = \phi^{Tx,Rx}$ )	$[-\pi, \pi]$
Focus angles ( $\theta_F^{Rx}, \phi_F^{Rx}$ )	$(60^\circ, 30^\circ)$

of the receiver, the performance of the SINR gets degraded depending on the severeness of the deviation.

In Fig. 7, the capacity of the system is shown for different AAOAs and EAOAs. As it can be seen from this figure, similar to Fig. 6, when the AAOAs and EAOAs are matched with the focus angles of the receiver, the capacity is maximized, whereas as the AAOAs' and EAOAs' deviation increases the capacity decreases accordingly.

In Fig. 8, the SINR performance of the proposed channel model is interrogated under the condition where both of the HAPs are mobile and the focus angle of the receiver is defined to be  $(\theta_F^{Rx}, \phi_F^{Rx}) = (60^\circ, 30^\circ)$ . As shown in Fig. 5, when the effect of Doppler is included due to mobility, there is a shift on the focus angles of the receiver, which leads the maximum beam gain to be achieved at a different set of angles rather than the desired one. Depending on the shift on the focus angles of the receiver, it is expected that the SINR performance of the system will not be maximized at the desired focus angles. As it can be seen from Fig. 8, even though the desired focus angles are defined to be  $(\theta_F^{Rx}, \phi_F^{Rx}) = (60^\circ, 30^\circ)$ , due to the Doppler, the maximum SINR is achieved at  $(\theta^{Rx}, \phi^{Rx}) = (47^\circ, 26^\circ)$ .

Fig. 9 shows the capacity of the system in the case where both of the HAPs are mobile and the focus angle of the receiver is defined to be  $(\theta_F^{Rx}, \phi_F^{Rx}) = (60^\circ, 30^\circ)$ . As it can be seen from this figure, while the performance of the SINR is expected to be higher at the angles  $(\theta^{Rx}, \phi^{Rx}) = (60^\circ, 30^\circ)$ , due to the mobility the focus angles are shifted and the SINR performance at the angles  $(\theta^{Rx}, \phi^{Rx}) = (47^\circ, 26^\circ)$  outperforms the SINR performance at the angles  $(\theta^{Rx}, \phi^{Rx}) = (60^\circ, 30^\circ)$ .

Fig. 10 and Fig. 11 show the SINR distribution of the proposed channel model for different deviations in the focus angle in those cases where the effect of Doppler due to mobility is omitted and included respectively. As it can be seen from Fig. 10, when the HAPs are stationary, the distribution of the SINR is gathering around smaller values as the deviations in AAOA and EAOA increases. In Fig. 11, the distribution of SINR is shown in the case where the HAPs are mobile. In this figure, even though the maximum SINR is expected to be achieved at the desired focus angles, due to the effect of Doppler, it is observed at a different set of angles.

In Fig. 12, a comparison between the proposed channel model and two other related works in the literature is given to emphasize the novelty of our work. The main difference that

is desired to be shown in this figure is the effect of mobility. The PDF of [10] shown in blue line is given for a low altitude UAV scenario where the UAVs are interrogated under hovering conditions. Moreover, the PDF of [37] illustrated in red line is given for a case where the opportunistic beamforming is performed in a multi-user scenario for a scheduled user with partial channel information. Even though the results given in [37] do not provide an analysis for A2A channel, it is still a proper comparison material to provide an insight for the evaluation of the difference between the stationary and mobile scenarios in beamforming applications. As it can be seen from the overall of this figure, the PDF of the SINR is lower at the two other scenarios because of the fact that the effect of ICI due to the mobility is not considered. However, when the effect of mobility is taken into account and compensated, the distribution of SINR increases accordingly.

## VI. CONCLUSION

In this paper, an analytical 3D channel model operating at mmWave band is proposed to represent the beamforming characteristics of HAPs in future 6G FANETs. In this regard, the MIMO characteristics of the two HAPs that are considered to be equipped with  $N \times N$  URPA antennas are interrogated in the presence of high mobility and its resultant Doppler shift. Moreover, a joint Gauss-Markov/3D random walk mobility model is introduced to provide a more accurate movement estimation of HAPs in real-life scenarios. The suggested model in this paper is proven by mathematical derivations and their validity is consolidated by Monte-Carlo simulations. The resulting outcomes from the obtained calculations and simulations in terms of SINR, capacity, gain, and PDF prove that the applicability of such communication that exploits beamforming in high frequencies between two mobile HAPs has a great potential to satisfy the requirements of future airborne NTN scenarios.

## REFERENCES

- [1] B. Li, Z. Fei, and Y. Zhang, "UAV communications for 5G and beyond: Recent advances and future trends," *IEEE Internet of Things Journal*, vol. 6, no. 2, pp. 2241–2263, 2018.
- [2] M. Kirik, N. A. Abusanad, and H. Arslan, "Inter-HAP based geometrical 3-D channel model operating at 28 to 60 GHz for future 6G non-terrestrial networks," in *IEEE Wireless Communications and Networking Conference (WCNC)*. IEEE, 2023, pp. 1–5.
- [3] Y. I. Demir, M. S. J. Solaija, and H. Arslan, "On the performance of handover mechanisms for non-terrestrial networks," in *IEEE 95th Vehicular Technology Conference:(VTC2022-Spring)*. IEEE, 2022, pp. 1–5.
- [4] Z. Zhang, Y. Xiao, Z. Ma, M. Xiao, Z. Ding, X. Lei, G. K. Karagiannidis, and P. Fan, "6G wireless networks: Vision, requirements, architecture, and key technologies," *IEEE Vehicular Technology Magazine*, vol. 14, no. 3, pp. 28–41, 2019.
- [5] L. Afeef and H. Arslan, "Beam squint effect in multi-beam mmWave massive MIMO systems," in *IEEE 96th Vehicular Technology Conference (VTC2022-Fall)*. IEEE, 2022, pp. 1–5.
- [6] X. Wang, L. Kong, F. Kong, F. Qiu, M. Xia, S. Arnon, and G. Chen, "Millimeter wave communication: A comprehensive survey," *IEEE Communications Surveys & Tutorials*, vol. 20, no. 3, pp. 1616–1653, 2018.
- [7] Z. Ma, B. Ai, R. He, G. Wang, Y. Niu, and Z. Zhong, "A wideband non-stationary air-to-air channel model for UAV communications," *IEEE Transactions on Vehicular Technology*, vol. 69, no. 2, pp. 1214–1226, 2019.

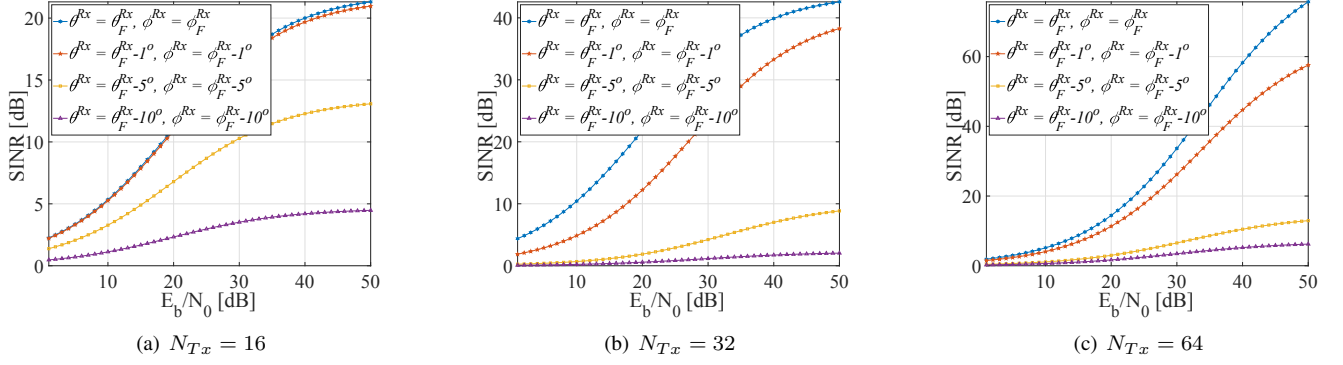


Fig. 6: SINR performance of the proposed channel model under different AAOs and EAOs when the effect of Doppler is neglected.

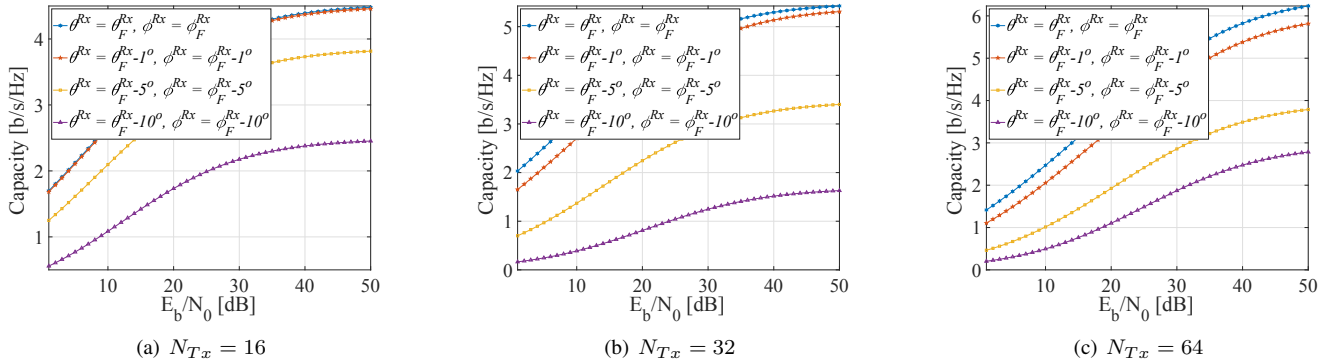


Fig. 7: Capacity of the proposed channel model under different AAOs and EAOs when the effect of Doppler is neglected.

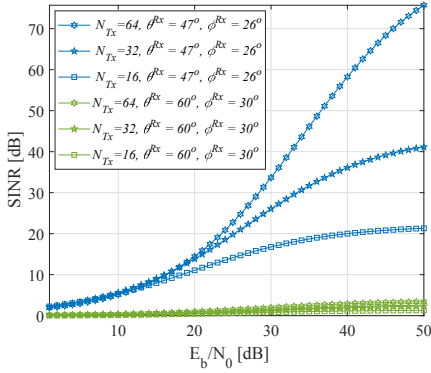


Fig. 8: SINR performance of the proposed channel model in the case where the HAPs are mobile and the focus angles are defined as  $(\theta_F^{Rx}, \phi_F^{Rx}) = (60^\circ, 30^\circ)$

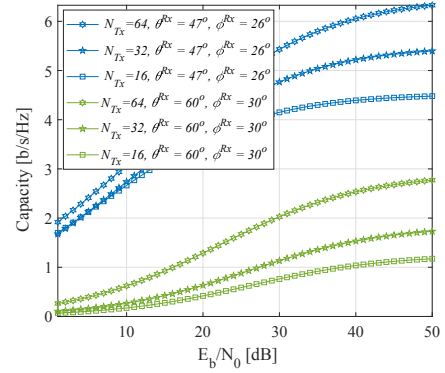


Fig. 9: Capacity performance of the proposed channel model in the case where the HAPs are mobile and the focus angles are defined as  $(\theta_F^{Rx}, \phi_F^{Rx}) = (60^\circ, 30^\circ)$

- [8] Z. Ma, B. Ai, R. He, Z. Zhong, M. Yang, J. Wang, L. Pei, Y. Li, and J. Li, "Three-dimensional modeling of millimeter-wave MIMO channels for UAV-based communications," in *GLOBECOM*. IEEE, 2020, pp. 1–6.
- [9] Z. Ma, B. Ai, R. He, Z. Zhong, and M. Yang, "A non-stationary geometry-based MIMO channel model for millimeter-wave UAV networks," *IEEE Journal on Selected Areas in Communications*, vol. 39, no. 10, pp. 2960–2974, 2021.
- [10] M. T. Dabiri, H. Safi, S. Parsaeefard, and W. Saad, "Analytical channel models for millimeter wave UAV networks under hovering fluctuations," *IEEE Transactions on Wireless Communications*, vol. 19, no. 4, pp. 2868–2883, 2020.
- [11] H. Jiang, Z. Zhang, and G. Gui, "Three-dimensional non-stationary wideband geometry-based UAV channel model for A2G communication environments," *IEEE Access*, vol. 7, pp. 26 116–26 122, 2019.
- [12] L. Zeng, X. Cheng, C.-X. Wang, and X. Yin, "A 3D geometry-based stochastic channel model for UAV-MIMO channels," in *IEEE Wireless Communications and Networking Conference (WCNC)*. IEEE, 2017, pp. 1–5.
- [13] X. Mao, C.-X. Wang, and H. Chang, "A 3D non-stationary geometry-based stochastic model for 6G UAV air-to-air channels," in *13th International Conference on Wireless Communications and Signal Processing (WCSP)*. IEEE, 2021, pp. 1–5.
- [14] H. Jiang, B. Xiong, H. Zhang, and E. Basar, "Physics-based 3D



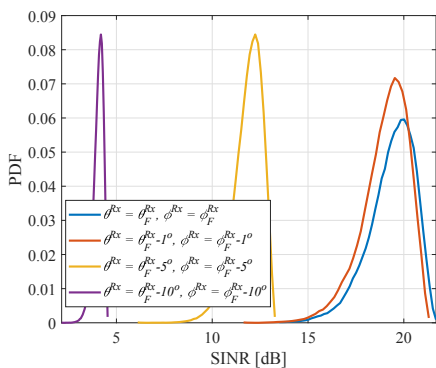


Fig. 10: PDF of the SINR under different AOA and EAOA deviations when  $N_{Tx} = 16$  and the effect of Doppler is neglected.

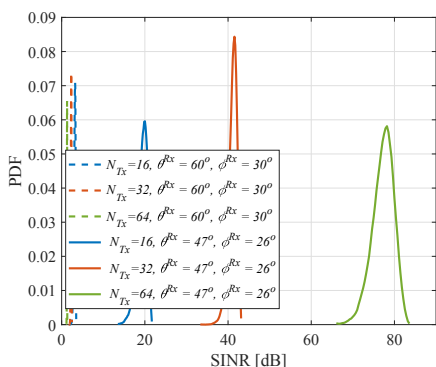


Fig. 11: PDF of the SINR in the case where the HAPs are mobile and the focus angles are defined as  $(\theta_F^{Rx}, \phi_F^{Rx}) = (60^\circ, 30^\circ)$ .

end-to-end modeling for double-RIS assisted non-stationary UAV-to-ground communication channels," *IEEE Transactions on Communications*, 2023.

- [15] C. Cao, Z. Lian, Y. Wang, Y. Su, and B. Jin, "A non-stationary geometry-based channel model for IRS-assisted UAV-MIMO channels," *IEEE Communications Letters*, vol. 25, no. 12, pp. 3760–3764, 2021.
- [16] Z. Lian, Y. Su, Y. Wang, and L. Jiang, "A non-stationary 3-D wideband channel model for intelligent reflecting surface-assisted HAP-MIMO communication systems," *IEEE Transactions on Vehicular Technology*, vol. 71, no. 2, pp. 1109–1123, 2021.
- [17] Z. Lian, L. Jiang, C. He, and Q. Xi, "A novel channel model for 3-D HAP-MIMO communication systems," in *International Conference on Networking and Network Applications (NaNA)*. IEEE, 2016, pp. 1–6.
- [18] Z. Lian, L. Jiang, C. He, and D. He, "A non-stationary 3-D wideband GBM for HAP-MIMO communication systems," *IEEE Transactions on Vehicular Technology*, vol. 68, no. 2, pp. 1128–1139, 2018.
- [19] B. Liang and Z. J. Haas, "Predictive distance-based mobility management for pcs networks," in *IEEE INFOCOM'99. Conference on Computer Communications. Proceedings. Eighteenth Annual Joint Conference of the IEEE Computer and Communications Societies. The Future is Now (Cat. No. 99CH36320)*, vol. 3. IEEE, 1999, pp. 1377–1384.
- [20] K.-H. Chiang and N. Shenoy, "A 2-D random-walk mobility model for location-management studies in wireless networks," *IEEE Transactions on Vehicular Technology*, vol. 53, no. 2, pp. 413–424, 2004.
- [21] T. Camp, J. Boleng, and V. Davies, "A survey of mobility models for ad hoc network research," *Wireless Communications and Mobile Computing*, vol. 2, no. 5, pp. 483–502, 2002.
- [22] J. Ariyakhajorn, P. Wannawilai, and C. Sathitwiriyaong, "A comparative study of random waypoint and Gauss-Markov mobility models in the performance evaluation of manet," in *International Symposium on*

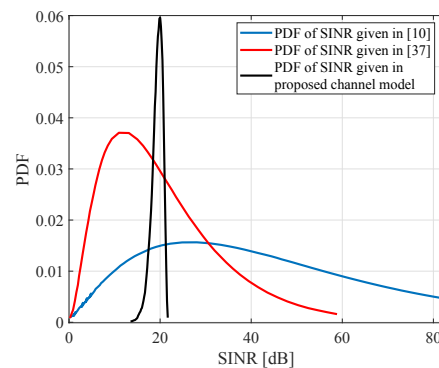


Fig. 12: PDF comparison of the proposed channel model with the related works in the literature.

*Communications and Information Technologies*. IEEE, 2006, pp. 894–899.

- [23] I. Bekmezci, O. K. Sahingoz, and Ş. Temel, "Flying ad-hoc networks (fanets): A survey," *Ad Hoc Networks*, vol. 11, no. 3, pp. 1254–1270, 2013.
- [24] P. Aguiar, D. Brett, and N. Brandon, "Solid oxide fuel cell/gas turbine hybrid system analysis for high-altitude long-endurance unmanned aerial vehicles," *International Journal of Hydrogen Energy*, vol. 33, no. 23, pp. 7214–7223, 2008.
- [25] Z. Ma, B. Ai, R. He, and Z. Zhong, "A 3D air-to-air wideband non-stationary channel model of UAV communications," in *90th Vehicular Technology Conference (VTC2019-Fall)*. IEEE, 2019, pp. 1–5.
- [26] W. Tan, S. D. Assimonis, M. Matthaiou, Y. Han, X. Li, and S. Jin, "Analysis of different planar antenna arrays for mmWave massive MIMO systems," in *85th Vehicular Technology Conference (VTC Spring)*. IEEE, 2017, pp. 1–5.
- [27] D. Tse and P. Viswanath, *Fundamentals of wireless communication*. Cambridge university press, 2005.
- [28] O. El Ayach, S. Rajagopal, S. Abu-Surra, Z. Pi, and R. W. Heath, "Spatially sparse precoding in millimeter wave MIMO systems," *IEEE Transactions on Wireless Communications*, vol. 13, no. 3, pp. 1499–1513, 2014.
- [29] S. Umeyama, "An eigendecomposition approach to weighted graph matching problems," *IEEE Transactions on Pattern Analysis and Machine Intelligence*, vol. 10, no. 5, pp. 695–703, 1988.
- [30] X. Yu, J. Zhang, M. Haenggi, and K. B. Letaief, "Coverage analysis for millimeter wave networks: The impact of directional antenna arrays," *IEEE Journal on Selected Areas in Communications*, vol. 35, no. 7, pp. 1498–1512, 2017.
- [31] N. Goddemeier and C. Wietfeld, "Investigation of air-to-air channel characteristics and a UAV specific extension to the rice model," in *2015 IEEE Globecom Workshops (GC Wkshps)*. IEEE, 2015, pp. 1–5.
- [32] S. Karapantazis and F. Pavlidou, "Broadband communications via high-altitude platforms: A survey," *IEEE Communications Surveys & Tutorials*, vol. 7, no. 1, pp. 2–31, 2005.
- [33] M. R. Akdeniz, Y. Liu, M. K. Samimi, S. Sun, S. Rangan, T. S. Rappaport, and E. Erkip, "Millimeter wave channel modeling and cellular capacity evaluation," *IEEE Journal on Selected Areas in Communications*, vol. 32, no. 6, pp. 1164–1179, 2014.
- [34] K. Ying, Z. Gao, S. Lyu, Y. Wu, H. Wang, and M.-S. Alouini, "GMD-based hybrid beamforming for large reconfigurable intelligent surface assisted millimeter-wave massive MIMO," *IEEE Access*, vol. 8, pp. 19 530–19 539, 2020.
- [35] R. He, C. Schneider, B. Ai, G. Wang, Z. Zhong, D. A. Dupleich, R. S. Thomae, M. Boban, J. Luo, and Y. Zhang, "Propagation channels of 5G millimeter-wave vehicle-to-vehicle communications: Recent advances and future challenges," *IEEE Vehicular Technology Magazine*, vol. 15, no. 1, pp. 16–26, 2019.
- [36] S. Li, B. Duo, X. Yuan, Y.-C. Liang, and M. Di Renzo, "Reconfigurable intelligent surface assisted UAV communication: Joint trajectory design and passive beamforming," *IEEE Wireless Communications Letters*, vol. 9, no. 5, pp. 716–720, 2020.
- [37] O. Ozdemir and M. Torlak, "Opportunistic beamforming over rayleigh channels with partial side information," *IEEE Transactions on Wireless Communications*, vol. 7, no. 9, pp. 3417–3427, 2008.